A GFEM-Based Reduced-Order Homogenization Model for Heterogeneous Materials under Volumetric and Interfacial Damage

David R. Brandyberry[1], Xiang Zhang[2,*], Philippe H. Geubelle[1]

[1]Department of Aerospace Engineering, University of Illinois at Urbana-Champaign

[2]Department of Mechanical Engineering, University of Wyoming

Abstract

This manuscript presents a multiscale reduced-order modeling framework for heterogeneous materials that accounts for both cohesive interface failure and continuum damage. The model builds on the eigendeformation-based reduced-order homogenization model (EHM), which relies on the pre-calculation of a set of coefficient tensors that account for the effects of linear and nonlinear material behavior between regions of the domain known as parts. A k-means clustering algorithm is used to optimally construct these parts and a new formulation for the partitioning of interfaces using this method is proposed. The extraction of the volumetric and interfacial influence functions is performed using the Interface-enriched Generalized Finite Element Method (IGFEM), which relies on a finite element discretization that does not conform to the material phase boundaries. A Lagrange multiplier method is used in this preprocessing phase, allowing for the reuse of the matrix factorization for different influence function problems and hence leading to efficiency improvement. A newly proposed traction calculation for the interface partition is also adopted to alleviate the instability caused by traction calculations along interfaces. The accuracy and efficiency of the IGFEM-EHM method is assessed through comparison with reference IGFEM simulations. The method is then used to extract the nonlinear multiscale response of particulate, unidirectional fiber-reinforced, and woven composites.

*Corresponding author. Tel.: +1 307 766 4238; Email address: xiang.zhang@uwyo.edu

Keywords— Eigendeformation-based Reduced-Order Homogenization Model, Generalized FEM, Composite Materials, Cohesive Model, Continuum Damage

1 Introduction

Composite materials demonstrate different failure modes including volumetric damage to the various phases and interfacial damage along the matrix/reinforcement interfaces [1]. From a numerical point of view, accounting for these different failure modes not only poses significant challenges in the modeling strategy (e.g., representation of continuum and interfacial damage), but also requires an efficient multiscale solution approach that bridges the response at the microstructure scale to that of the structural scale.

Computational homogenization has been effectively used to determine effective elastic [2, 3, 4, 5] and inelastic [6] responses of representative periodic unit cells (PUCs), providing a method of upscaling the response of a fully resolved microstructure to that of a material point at the macroscale [7, 8, 9]. While homogenization techniques have been successfully applied to a wide range of materials and physical phenomena (e.g., see review in [10]), using direct computational homogenization for structural scale simulation still remains computationally prohibitive even with massive parallelization [11] and efficient solver methodologies [12].

To alleviate the computational cost associated with computational homogenization, different strategies have been adopted in the literature with a focus on model-order reduction of the microscale problem, including the proper orthogonal decomposition [13, 14], fast Fourier transform [15] and its extension to incorporate interface decohesion [16], self-consistent clustering analysis [17, 18], data driven modeling [19] and its interfacial failure formulation [20], transformation field analysis (TFA) [6] and its nonuniform extension (NTFA) [21]. The eigendeformation-based reduced-order homogenization model (EHM), which is based on TFA, provides a hierarchical model-order reduction strategy for heterogeneous materials [22, 23], and has been further advanced to model different constituents in the presence of plasticity [24, 25, 26, 27, 28] and/or damage (both continuum and discrete) [29, 30]. EHM allows for efficient modeling of the inelastic behavior of complex microstructures, but the elastic components of the microstructure response must be precomputed using other methods in its preprocessing stage. In addition, the application of EHM for composite materials and structures has so far been mostly limited to relatively simple microstructures (e.g., a single inclusion), and the capability to handle large and complex microstructures with the presence of multiple failure modes is still to be demonstrated.

Many methods may be used to evaluate the elastic response of a given microstructure including the standard Finite Element Method (FEM) or other Generalized Finite Element Methods (GFEM). Due to its ability to capture complex microstructures by incorporating

non-conforming meshes and intuitive enrichment functions, the Interface-enriched Generalized Finite Element Method (IGFEM) [31] has been selected for the preprocessing stage in this work.

This manuscript builds on the ideas of EHM and introduces the following contributions: (i) The elastic preprocessing stage is conducted using the IGFEM, which allows for modeling of many geometries with a single finite element discretization; (ii) A Lagrange multiplier method is adopted for the preprocessing step to solve the influence functions corresponding to each interface partition, thereby allowing for the re-use of the stiffness matrix factorization and vastly improving the EHM preprocessing efficiency; (iii) A new average traction formulation for the interface parts is proposed, which eliminates stability issues with the IGFEM-based EHM when interfacial cohesive failure [32, 33, 34] is considered; (iv) The clustering scheme proposed in [17] is extended for interface partitioning and is shown to greatly speed up the convergence of the IGFEM-EHM scheme, even for large and complex microstructures.

This manuscript is organized as follows: Section 2 starts with an overview of the EHM, then proceeds with its integration with IGFEM focusing on both the preprocessing stage and the formation of the reduced-order system with emphasis on the new treatment of the traction formulation. The clustering method for the generation of the phase parts and its extension to the interfacial parts are also presented in that section. Section 3 covers the phase and interface inelastic models considered in the remainder of the manuscript. Section 4 conducts a systematic verification study of the convergence of the solution from the IGFEM-EHM scheme for the cases of inclusion damage, matrix damage, and cohesive failure. The proposed method is applied to several complex microstructures in Section 5, and Section 6 summarizes this manuscript and proposes future research directions.

2 IGFEM-Based EHM

This section summarizes the existing EHM method that accounts for nonlinear responses in the matrix and reinforcement phases and along the material interfaces of composite materials, and details the use of IGFEM in conjunction with a Lagrange multiplier scheme for efficient preprocessing. A novel traction homogenization scheme is then proposed to compute the reduced-order system of equations.

The standard computational homogenization problem seeks to evaluate the mechanical response of a material through the direct homogenization of the stress field in a unit cell problem over the domain Θ subject to a macroscopic strain loading $\bar{\boldsymbol{\epsilon}}$. The macroscopic strain is assumed to be constant over Θ in accordance with the separation-of-scales assumption. The response of this microscale domain is governed by

$$
\begin{aligned}
&\sigma_{ij,j}\left(\boldsymbol{\epsilon}\left(\boldsymbol{y}\right)\right)=0, \qquad \boldsymbol{y}\in\Theta\\
&\epsilon_{ij}\left(\boldsymbol{y}\right)=\bar{\epsilon}_{ij}+\tilde{\epsilon}_{ij}\left(\boldsymbol{y}\right),\\
&\tilde{\epsilon}_{ij}\left(\boldsymbol{y}\right)=\frac{1}{2}\left(\tilde{u}_{i,j}+\tilde{u}_{j,i}\right),\\
&\sigma_{ij}\left(\boldsymbol{y}\right)n_j\left(\boldsymbol{y}\right)=t_i\left(\left[\!\left[\tilde{\boldsymbol{u}}\left(\boldsymbol{y}\right)\right]\!\right]\right), \qquad \boldsymbol{y}\in\Gamma\\
&\bar{\sigma}_{ij}=\frac{1}{|\Theta|}\int_{\Theta}\sigma_{ij}\left(\boldsymbol{y}\right)d\Theta,
\end{aligned}
\tag{1}
$$

where the strain tensor ϵ_{ij} has been decomposed into contributions from the macroscale component $\bar{\epsilon}_{ij}$ and a perturbation value $\tilde{\epsilon}_{ij}$ defined as the symmetric gradient of the perturbation displacement $\tilde{u}_i$, which is periodic in Θ. $|\cdot|$ operator indicates the volume (3D) or area (2D) of Θ. $f_{,i}$ denotes partial derivative of f with respect to y_i. Additionally, the fourth equation in (1) relates the cohesive tractions, t_i, caused by jumps in $\tilde{\boldsymbol{u}}$ along material interfaces, Γ, to the local stress field and the interface normal vector n_j. The final equation in (1) relates the local stresses σ_{ij} to the macroscopic stress $\bar{\sigma}_{ij}$.

As a point of departure to the conventional computational homogenization, EHM seeks a reduced representation of the full-field microscale problem. EHM expresses the perturbation displacement in terms of *influence functions*, which are numerical Green's functions computed by solving linear elastic problems defined over the microstructure domain. The inelastic fields within the microstructure (or eigendeformation in the context of TFA [6, 35]) are approximated by a coarse discretization associated with subdomains, referred to as *reduced-order parts*, of the microstructure. Specifically, the volume of the microstructure that is damageable is partitioned into $\tilde{M}$ parts denoted by $\Theta^{[\alpha]}$, $\alpha=1,2...,\tilde{M}$, and all the material interfaces are partitioned into $\breve{M}$ interfacial parts denoted by $\Gamma^{[\xi]}$, $\xi=1,2...,\breve{M}$. All phase and interfacial parts are non-overlapping (i.e., $\Theta^{[\alpha]}\cap\Theta^{[\beta]}=\emptyset$ for $\alpha\neq\beta$, $\Gamma^{[\xi]}\cap\Gamma^{[\eta]}=\emptyset$ for $\xi\neq\eta$). The perturbation displacement field from (1) is then approximated by

$$
\tilde{u}_i(\boldsymbol{y})=H_i^{kl}(\boldsymbol{y})\bar{\epsilon}_{kl}+\sum_{\xi=1}^{\breve{M}}\breve{h}_i^{n[\xi]}(\boldsymbol{y})\delta_n^{[\xi]}+\sum_{\xi=1}^{\tilde{M}}\tilde{h}_i^{kl[\alpha]}(\boldsymbol{y})\mu_{kl}^{([\alpha]}, \tag{2}
$$

which is a linear combination of the elastic ($\boldsymbol{H}$), phase inelastic ($\tilde{\boldsymbol{h}}$) and interface inelastic ($\breve{\boldsymbol{h}}$) influence functions that will be derived in Section 2.1. $\delta_n^{[\xi]}$ is the displacement jump on interface part ξ and $\mu_{kl}^{([\alpha]}$ is the inelastic strain in phase part α.

Employing the microscale displacement discretization and the assumed spatial variance of the inelastic response in the microstructure (e.g., piecewise constant over each part), the microscale governing equations are converted to an algebraic system that is solved for the small set of eigenstrain coefficients for each volume part, and of eigenseparation coefficients for each interfacial part. The detailed derivation of the reduced-order model (ROM) system

can be found in [22, 23], leading to the following form of the ROM system that replaces the full-field microscale problem:

$$E_{ij}^{kl[\beta]}\bar{\epsilon}_{kl} + \sum_{\alpha=1}^{\tilde{M}} P_{ij}^{kl[\beta\alpha]}\mu_{kl}^{[\alpha]}(\boldsymbol{\epsilon}^{[\alpha]}) + \sum_{\xi=1}^{\breve{M}} O_{ij}^{m[\beta\xi]}\delta_m^{[\xi]} - \epsilon_{ij}^{[\beta]} = 0, \tag{3a}$$

$$t_n^{[\eta]}(\boldsymbol{\delta}^{[\eta]}) - \sum_{\alpha=1}^{\tilde{M}} C_n^{kl[\eta\alpha]}\mu_{kl}^{[\alpha]}(\boldsymbol{\epsilon}^{[\alpha]}) - \sum_{\xi=1}^{\breve{M}} D_n^{m[\eta\xi]}\delta_m^{[\xi]} - T_n^{kl[\eta]}\bar{\epsilon}_{kl} = 0, \tag{3b}$$

where $\boldsymbol{\mu}^{[\alpha]}(\boldsymbol{\epsilon}^{[\alpha]})$ is a nonlinear material model for the inelastic strain caused by the total strain in part α, $\boldsymbol{\epsilon}^{[\alpha]}$. The nonlinear cohesive zone model $\boldsymbol{t}^{[\eta]}(\boldsymbol{\delta}^{[\eta]})$ gives the traction on part η caused by the local displacement jump $\boldsymbol{\delta}^{[\eta]}$. The $\boldsymbol{E}$, $\boldsymbol{P}$, and $\boldsymbol{O}$ tensors are the concentration and interaction tensors acting on a phase part β,

$$\begin{aligned}
E_{ij}^{kl[\beta]} &= \frac{1}{\left|\Theta^{[\beta]}\right|}\int_{\Theta^{[\beta]}} H_{(i,y_j)}^{kl}(\boldsymbol{y})d\Theta + I_{ijkl}, \\
P_{ij}^{kl[\beta\alpha]} &= \frac{1}{\left|\Theta^{[\beta]}\right|}\int_{\Theta^{[\beta]}} \tilde{h}_{(i,y_j)}^{kl[\alpha]}(\boldsymbol{y})d\Theta, \\
O_{ij}^{m[\beta\xi]} &= \frac{1}{\left|\Theta^{[\beta]}\right|}\int_{\Theta^{[\beta]}} \breve{h}_{(i,y_j)}^{m[\xi]}(\boldsymbol{y})d\Theta,
\end{aligned} \tag{4}$$

while the $\boldsymbol{T}$, $\boldsymbol{C}$, and $\boldsymbol{D}$ tensors are the concentration and interaction tensors acting on an interface part ξ expressed as

$$\begin{aligned}
T_n^{kl[\eta]} &= \frac{1}{\left|\Gamma^{[\eta]}\right|}\int_{\Gamma^{[\eta]}} Q_{ni}(\boldsymbol{y})L_{ijpq}(\boldsymbol{y})\left[H_{(p,y_q)}^{kl}(\boldsymbol{y}) + I_{pqkl}(\boldsymbol{y})\right]\bar{n}_j(\boldsymbol{y})d\Gamma, \\
C_n^{kl[\eta\alpha]} &= \frac{1}{\left|\Gamma^{[\eta]}\right|}\int_{\Gamma^{[\eta]}} Q_{ni}(\boldsymbol{y})L_{ijpq}(\boldsymbol{y})\left[\tilde{h}_{(p,y_q)}^{kl[\alpha]}(\boldsymbol{y}) - I_{pqkl}^{[\alpha]}(\boldsymbol{y})\right]\bar{n}_j(\boldsymbol{y})d\Gamma, \\
D_n^{m[\eta\xi]} &= \frac{1}{\left|\Gamma^{[\eta]}\right|}\int_{\Gamma^{[\eta]}} Q_{ni}(\boldsymbol{y})L_{ijpq}(\boldsymbol{y})\breve{h}_{(p,y_q)}^{m[\xi]}(\boldsymbol{y})\bar{n}_j(\boldsymbol{y})d\Gamma.
\end{aligned} \tag{5}$$

In (5), Q_{ik} is an orthogonal transformation matrix defined by the material interface geometry which transforms the vector into a local coordinate system on the interface surface and $\bar{n}_j$ is the interface unit normal vector. All the coefficient tensors (i.e., $\boldsymbol{E}$, $\boldsymbol{P}$, $\boldsymbol{O}$, $\boldsymbol{T}$, $\boldsymbol{C}$ and $\boldsymbol{D}$) are functions of the influence functions, which are computed in the preprocessing stage for a given microstructure and ROM partitioning.

After the above ROM system is solved, the macroscale stresses are computed as an average over the PUC as

$$\bar{\sigma}_{ij} = \bar{L}_{ijkl}\bar{\epsilon}_{kl} + \sum_{\alpha=1}^{\tilde{M}} \bar{A}_{ijkl}^{[\alpha]}\mu_{kl}^{[\alpha]} + \sum_{\xi=1}^{\breve{M}} \bar{B}_{ijn}^{[\xi]}\delta_n^{[\xi]}, \tag{6}$$

where

$$\bar{L}_{ijkl} = \frac{1}{|\Theta|}\int_{\Theta} L_{ijpq}(\boldsymbol{y})\left[H^{kl}_{(p,y_q)}(\boldsymbol{y}) + I_{pqkl}(\boldsymbol{y})\right] d\Theta,$$
$$\bar{A}^{[\alpha]}_{ijkl} = \frac{1}{|\Theta|}\int_{\Theta} L_{ijpq}(\boldsymbol{y})\left[\tilde{h}^{kl[\alpha]}_{(p,y_q)}(\boldsymbol{y}) - I^{[\alpha]}_{pqkl}(\boldsymbol{y})\right] d\Theta, \tag{7}$$
$$\bar{B}^{[\xi]}_{ijn} = \frac{1}{|\Theta|}\int_{\Theta} L_{ijkl}(\mathbf{y})\breve{h}^{n[\xi]}_{k,y_l}(\mathbf{y}) d\Theta.$$

$I^{[\alpha]}_{pqkl}$ is the piecewise constant identity tensor defined in (9). Equations (3) - (7), together with constitutive equations for the nonlinear phase parts and traction-separation laws for the interface parts, complete the ROM formulation. This ROM can be used to investigate the response of a microstructure under a prescribed macroscale loading history. Alternatively, the ROM can serve as a constitutive equation of a material point of the macroscale problem in a coupled multiscale analysis, but this manuscript focuses on the former.

2.1 Influence functions calculation using IGFEM

IGFEM efficiently models complex heterogeneous microstructures due to its use of finite-element discretizations that do not conform to the internal microstructure geometry and to its intuitive introduction of enrichment functions. The method relies on enriched degrees of freedom placed along the intersection of the material interfaces with the non-conforming background mesh (Figure 1). The intersected elements are split into subdomains called *integration elements* where the shape functions associated with the enriched degrees of freedom are defined. The Lagrange shape functions of the integration elements are typically used as enrichment functions, which has the advantages over other GFEM methods of simplicity and of vanishing at the non-enrichment nodes, allowing for easy application of Dirichlet boundary conditions. For more details on IGFEM, see [36, 37]. The IGFEM can also be used to capture interfacial debonding [38, 39, 40, 41, 42] by introducing two superposed nodes at each interface-mesh intersection point as shown in Figure 1b. As shown hereafter, a standard application of the IGFEM to the influence function governing equations, combined with a Lagrange multiplier scheme, can be used to solve the influence function problems efficiently.

Influence function problems are directly derived from the microscale equilibrium by different combinations of the eigenstrains and eigenseparations, ensuring automatic satisfaction of the microscale equilibrium as detailed in [22] and summarized here for completeness. The Elastic Influence Function (EIF) problem represents the response of the elastic microstructure under unit macroscopic strains with perfect interfaces and is described by

$$\left\{L_{ijmn}(\boldsymbol{y})\left(I_{mnkl} + H^{kl}_{(m,y_n)}(\boldsymbol{y})\right)\right\}_{,y_j} = 0 \qquad \boldsymbol{y} \in \Theta. \tag{8}$$

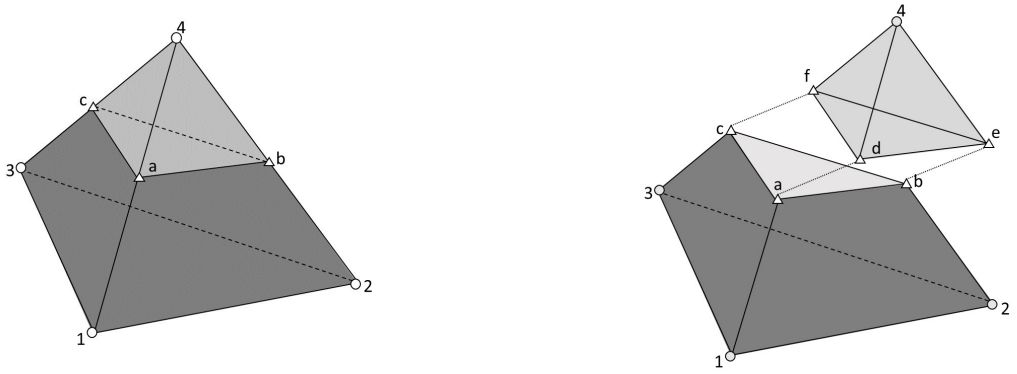

(a) Perfect interface (b) Cohesive interface

Figure 1: 4-node tetrahedral element intersected by one (a) perfect material interface and (b) cohesive material interface. The IGFEM formulation can be expanded to non-conforming elements intersected by multiple interfaces [43].

This elastic problem is readily solved using IGFEM by successively enforcing a unit macroscopic strain loading for each component of $\bar{\boldsymbol{\epsilon}}$. The resulting periodic solution field, $H_i^{kl}(\boldsymbol{y})$, is the perturbation displacement component i induced by the unit strain component $\bar{\epsilon}_{kl}$.

Similarly, the Phase Influence Function (PIF) problem represents the response in each phase part due to a unit eigenstrain acting in part α for the elastic microstructure with perfect interfaces and is expressed as

$$\begin{gathered}\left\{L_{ijmn}(\boldsymbol{y})\left(\tilde{h}^{kl[\alpha]}_{(m,y_n)}(\boldsymbol{y}) - I^{[\alpha]}_{mnkl}(\boldsymbol{y})\right)\right\}_{,y_j} = 0, \qquad \boldsymbol{y} \in \Omega \qquad \forall \alpha \\ I^{[\alpha]}_{mnkl}(\boldsymbol{y}) = \begin{cases} I_{mnkl} & \boldsymbol{y} \in \Theta^{[\alpha]} \\ \mathbf{0} & \text{otherwise} \end{cases} .\end{gathered} \tag{9}$$

This problem can again be solved for each phase part by imposing negative unit macroscopic strains acting in each phase part α and computing the resulting periodic perturbation displacements, giving the PIF $\tilde{h}_i^{kl[\alpha]}$ for part α subject to unit inelastic strains μ_{kl}. For three-dimensional problems, this involves solving $6 \cdot \tilde{M}$ linear finite element problems. However, all PIF problems have the same tangent stiffness matrix so they can be computed very efficiently using a direct matrix factorization.

The Interface Influence Function (IIF) problem describes the effect of a unit displacement jump opening on a given interface part ξ on the surrounding elastic field. This problem is given by

$$\begin{aligned}\left\{L_{ijkl}(\boldsymbol{y})\breve{h}^{m[\xi]}_{(k,y_l)}(\boldsymbol{y})\right\}_{,y_j} &= 0, \qquad \boldsymbol{y}\in\Theta \qquad \forall\xi \\ Q_{ik}(\boldsymbol{y})[\![\breve{h}^{m[\xi]}_{k}(\boldsymbol{y})]\!] &= \delta_{im}\sum_{n\in\Gamma^{[\xi]}} N^e_n(\boldsymbol{y}) \qquad \boldsymbol{y}\in\Gamma^{[\xi]}.\end{aligned} \tag{10}$$

Q_{ik} is the same transformation matrix introduced in (5) and δ_{im} is the Kronecker Delta. N^e_n are the cohesive element shape function corresponding to nodes that are part of interface part ζ. This sum of shape functions enforces a displacement jump solution that is C^0-continuous for standard Lagrange shape functions rather than fully piecewise constant. The IIF, $\breve{h}^{m[\xi]}_k(\boldsymbol{y})$, is the resulting periodic perturbation displacement field.

Previous work [22, 23, 44] recommends inserting mirror nodes to all current interface part nodes while enforcing perfect interfaces elsewhere by eliminating the mirror nodes along these perfect interfaces. This approach has the disadvantage of modifying the stiffness matrix for the evaluation of every IIF problem and requires refactoring the stiffness matrix each time. An alternative method is adopted here that allows us to reuse the full matrix factorization for every EIF, PIF, and IIF calculation. Node pairs are included for all material interface-mesh intersection points as in Figure 1b and constraints are imposed on the displacement jumps across these node pairs:

$$g^n_i = Q_{ij}(\boldsymbol{y}^n)[\![\tilde{u}^n_j]\!] - \Delta^{n*}_i = 0 \qquad \forall n\in\Gamma, \tag{11}$$

where $\tilde{u}^n_j$ is the j^{th} component of the EIF, PIF, or IIF on the given interface node-pair n, and Δ^{n*}_i is the prescribed displacement jump in the i^{th} direction. For EIF and PIF calculations, this value is always 0. For the IIF problem for $\breve{h}^{m[\xi]}_j$, $\Delta^{n*}_i = 1$ if $n\in\Gamma^{[\xi]}$ and if $i=m$.

These constraints can be expressed in matrix form as

$$\begin{aligned}\boldsymbol{g} = \boldsymbol{G}\tilde{\boldsymbol{U}} - \boldsymbol{\Delta}^* &= 0, \\ \boldsymbol{G} &= \mathop{\mathbf{A}}_{n\in\Gamma}\boldsymbol{Q}(\boldsymbol{y}^n), \\ \boldsymbol{\Delta}^* &= \mathop{\mathbf{A}}_{n\in\Gamma}\boldsymbol{\Delta}^{n*},\end{aligned} \tag{12}$$

allowing us to form the Lagrangian

$$\mathbb{L}\left(\tilde{\boldsymbol{U}},\boldsymbol{\Lambda}\right) = \frac{1}{2}\left(\bar{\boldsymbol{U}}+\tilde{\boldsymbol{U}}\right)^T\boldsymbol{K}\left(\bar{\boldsymbol{U}}+\tilde{\boldsymbol{U}}\right) + \boldsymbol{\Lambda}^T\boldsymbol{g}, \tag{13}$$

where the full finite element displacement vector is split into its perturbation portion $\tilde{\boldsymbol{U}}$ and the contribution from the macroscopic loading $\bar{\boldsymbol{U}}$. Λ is the vector of Lagrange multipliers. $\boldsymbol{K}$ is the linear portion of the finite element stiffness matrix and $\tilde{\boldsymbol{U}}$ can be the solution of any

of the influence function problems presented in (8), (9), or (10). Minimizing this Lagrangian leads to the system of linear equations

$$\begin{bmatrix} \boldsymbol{K} & \boldsymbol{G}^T \\ \boldsymbol{G} & \boldsymbol{0} \end{bmatrix} \begin{Bmatrix} \tilde{\boldsymbol{U}} \\ \boldsymbol{\Lambda} \end{Bmatrix} = \begin{Bmatrix} -\boldsymbol{P} \\ \boldsymbol{\Delta}^* \end{Bmatrix}, \tag{14}$$

for all influence function problems.

For the EIF problem, $\boldsymbol{H}^{kl}$, the internal load is

$$\boldsymbol{P}^{kl} = \underset{e \in \Theta}{\mathbf{A}} \int_{\Theta_e} \boldsymbol{B}^T v(L_{ijkl}) d\Theta \tag{15}$$

while the constraint vector $\boldsymbol{\Delta}^* = \boldsymbol{0}$. Here e indicates element number, and Θ_e denotes the domain associated with element e. $\boldsymbol{B}$ is the standard arrangement of finite element shape function gradients, and $v(\cdot)$ operator represents transformation of the high-order tensor to Voigt notation. For the PIF problem, $\tilde{\boldsymbol{h}}^{kl[\alpha]}$, the constraint vector is also equal to $\boldsymbol{0}$ while the internal load is

$$\boldsymbol{P}^{kl[\alpha]} = - \underset{e \in \Theta^{[\alpha]}}{\mathbf{A}} \int_{\Theta_e} \boldsymbol{B}^T v(L_{ijkl}) d\Theta. \tag{16}$$

For the IIF problem, $\breve{\boldsymbol{h}}^{m[\xi]}$, the internal load is $\boldsymbol{0}$ but the constraint vector is

$$\boldsymbol{\Delta}^{*m[\xi]} = \underset{n \in \Gamma^{[\xi]}}{\mathbf{A}} \delta_{im}. \tag{17}$$

In this vector assembly, every interface node-pair of the interface part ξ is assigned a local displacement jump opening with a single nonzero entry in the m^{th} location.

2.2 Reduced traction integration

The formulation of averaging the traction vector along interface parts in (5) is identical to the formulation presented in [44], but it may create an unstable system when the influence functions are solved via IGFEM due to the presence of sliver integration elements along interfaces. These sliver elements have poor stress solutions due to the ill-conditioning of the finite element stiffness matrix and, when these stresses are directly used to average a surface traction, the resulting ROM system may become unstable. Instead, rather than calculating the traction directly from the influence functions, the nodal forces from the IGFEM solution of the influence functions can be reused to evaluate the integrals:

$$
\begin{aligned}
T_n^{kl[\eta]} &= -\frac{1}{\left|\Gamma^{[\eta]}\right|}\sum_{p\in\Gamma^{[\eta]}} Q_{ni}(\boldsymbol{y}^p)\,{}^pF_i^{kl},\\
C_n^{kl[\eta\alpha]} &= -\frac{1}{\left|\Gamma^{[\eta]}\right|}\sum_{p\in\Gamma^{[\eta]}} Q_{ni}(\boldsymbol{y}^n)\,{}^pF_i^{kl[\alpha]},\\
D_n^{m[\eta\xi]} &= -\frac{1}{\left|\Gamma^{[\eta]}\right|}\sum_{p\in\Gamma^{[\eta]}} Q_{ni}(\boldsymbol{y}^n)\,{}^pF_i^{m[\xi]}.
\end{aligned}
\tag{18}
$$

The nodal forces at all points p in the interface part η are transformed to local coordinates by the transformation matrix $\boldsymbol{Q}$ at point p and summed. They are then averaged over the area of the interface. The internal forces are calculated from the loads in (15) and (16) and by integration of the appropriate influence functions as

$$
\begin{aligned}
\boldsymbol{F}^{ij} &= \mathop{\mathbf{A}}_{e\in\Theta}\int_{\Theta_e} \boldsymbol{B}^T v\Big(L_{pqkl}H^{ij}_{(k,y_l)}\Big)d\Theta + \boldsymbol{P}^{ij},\\
\boldsymbol{F}^{ij[\alpha]} &= \mathop{\mathbf{A}}_{e\in\Theta}\int_{\Theta_e} \boldsymbol{B}^T v\Big(L_{pqkl}\tilde{h}^{ij[\alpha]}_{(k,y_l)}\Big)d\Theta + \boldsymbol{P}^{ij[\alpha]},\\
\boldsymbol{F}^{m[\xi]} &= \mathop{\mathbf{A}}_{e\in\Theta}\int_{\Theta_e} \boldsymbol{B}^T v\Big(L_{pqkl}\check{h}^{m[\xi]}_{(k,y_l)}\Big)d\Theta.
\end{aligned}
\tag{19}
$$

The evaluation of (5) by volume integrals rather than surface integrals leads to a stable ROM system because the nodal forces are guaranteed to be in static equilibrium by the definition of the influence function problems which are solve via IGFEM. The traction integrals from (5) are a post-processing step and thus do not have the same guarantee.

2.3 Domain partitioning

Many ROMs rely on representing the microscale problem using a small number of functions spanning a basis with dimensions much smaller than the full microscale problem. Choosing the appropriate basis, as well as the order that can represent the fine scale response, is therefore critical. In EHM, this choice consists of splitting the damageable phase regions and imperfect interfaces into a desired number of parts, and selecting their geometries. Increasing the number of parts decreases the model error but also increases the computational cost. It is therefore desirable to achieve the lowest error using the fewest number of parts. While the concept of dynamic partitioning to achieve adaptive model order refinement on the fly is proposed in [22], most studies adopt a static partitioning defined in the preprocessing that is kept unchanged in the nonlinear analysis. Partitioning can be based on the geometry or the mechanical response

of the microstructure. In the geometry-based partitioning, geometrical features such as internal inclusion geometries in particulate composites or grains in polycrystalline metals are used to partition the microstructures [45, 46, 47, 48, 49, 50]. In response-based partitioning, the microstructure is subjected to a given loading, and sub-domains of the microstructure with similar responses are grouped into the same parts [17, 18]. Optimization can also be used to determine the optimal partitioning of the microstructure [51, 52]. To that end, the response-based partitioning scheme for phases described in [17] is adopted here and further extended to interface partitioning. A k-means clustering algorithm is used to optimally form groups of elements and nodes that behave similarly in their elastic response, which ensures that the assumptions of uniform inelastic strains and displacement jump openings that were made in the ROM formulation will produce minimal errors for a set number of parts.

The strain concentration tensor, $A_{ijkl}(\boldsymbol{y})$, defined at each integration point as

$$\epsilon_{ij}(\boldsymbol{y}) = A_{ijkl}(\boldsymbol{y})\bar{\epsilon}_{kl} \tag{20}$$

is utilized to determine how similarly elements behave and is obtained from the elastic influence function problem. This tensor is then averaged in each element using Gauss quadrature. Examples of the difference between geometry-based partitioning and this clustering partitioning of the phase region can be found in [17]. While for standard FEM, entire elements are grouped together into phase parts, *integration elements* (as depicted in Fig. 1) are grouped when using IGFEM.

To extend this partitioning scheme for interfaces, a similar measure for the interfacial parts is the displacement jump opening at each interface node-pair. To cluster by displacement jumps, an additional elastic problem must thus be solved where the constraints in (11) are not applied and a linear cohesive law with stiffness equal to the initial stiffness of the nonlinear cohesive zone model (CZM) is applied to cohesive surfaces. Equation (8) is then solved with the inclusion of these cohesive elements and the displacement jump openings for each load component are recorded, leading to a displacement jump concentration matrix $J_{nij}(\boldsymbol{y})$ introduced as

$$\delta_n(\boldsymbol{y}) = J_{nij}(\boldsymbol{y})\bar{\epsilon}_{ij}, \tag{21}$$

which is defined at each interface node-pair. This value is then used to cluster interface node pairs into interface parts. Figure 2 shows the difference between a geometry-based partitioning and a clustering-based partitioning of the interface of a simple single sphere geometry. While the geometry-based partitioning assumes that adjacent regions have a similar opening response, the clustering method ensures this and allows disconnected areas to belong to the same part.

In three dimensions, the A matrix is 6x6 and the J matrix is 3x6 when Voigt notation is used. In this work only the columns corresponding to nonzero components of the applied

macroscopic loads are considered, but in general a full representation of the A and J matrices can be considered to generate a partitioning that robustly models responses to many load cases.

$A_{ijkl}(\boldsymbol{y})$ and $J_{nij}(\boldsymbol{y})$ are clustered using the standard Lloyd's algorithm, which iteratively finds the centroid of each cluster of data, and then re-partitions based on which centroid is closest to each data point until the cluster assignments cease to change [53]. The quality of the partitioning produced by this algorithm strongly depends on starting with a representative set of cluster centroids for the initial assignment. For this reason, the k-means++ algorithm [54] is employed to seed the initial centroids and $n_{cluster}$ data points are randomly selected with preference given to points far away from those previously selected.

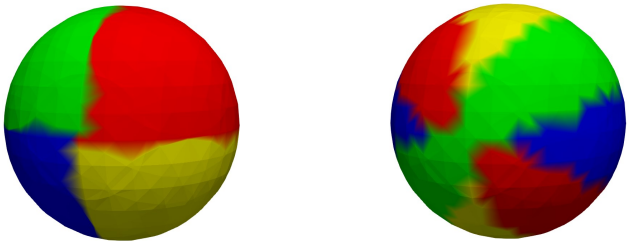

(a) (b)

Figure 2: Example partitioning of the the cohesive interface around a spherical inclusion using four parts. (a) A geometry-based partitioning. (b) Partitioning based on clustering of displacement jump openings.

3 Nonlinear Damage Models

The two material nonlinearities that are examined in this work are cohesive debonding of material interfaces and continuum damage inside of reinforcement phases as well as in the surrounding matrix. This combination of models is able to capture a rich set of homogenized material behaviors and the specific choice of traction and damage models chosen here may readily be interchanged with others.

3.1 Cohesive interface model

The traction-separation behavior of material interfaces is modeled using the exponential cohesive-zone model (CZM) of Ortiz and Pandolfi [32], which relies on a scalar effective representation of the displacement jump vector

$$\delta_e = \sqrt{\beta^2 \delta_s^2 + \delta_n^2}, \tag{22}$$

where δ_n is the normal component of the displacement jump vector and δ_s is the shear opening magnitude. β allows for weighting the normal and shear components separately but is kept as 1 for this work. This effective displacement jump induces a scalar traction given by

$$t = \frac{\sigma_c}{\delta_c}\left(\zeta\dot{\delta}_e + \delta_e \exp\left[(1-\delta^*/\delta_c)\right]\right), \quad \delta^* = \begin{cases} \delta_e & \text{if } \delta_e \geq \delta_{max} \\ \delta_{max} & \text{otherwise} \end{cases} \tag{23}$$

and is used to evaluate the complete traction vector

$$\mathbf{t} = \frac{t}{\delta_e}[\beta^2\,\boldsymbol{\delta} + (1-\beta^2)\delta_n \boldsymbol{n}]. \tag{24}$$

$\boldsymbol{\delta}$ is the displacement jump vector and $\boldsymbol{n}$ is the unit interface normal vector. Small values of the critical displacement jump opening, δ_c, relative to the domain size can lead to convergence difficulties in the nonlinear solution process, which are solved here through the inclusion of a numerical damping term in (23). The time-derivative $\dot{\delta}_e$ is computed by a backward difference and the coefficient ζ is kept small ($\sim 10^{-5}$ s) to minimize its impact on the solution. Equation (23) also introduces linear unloading through the use of the internal variable δ_{max} to avoid unrealistic healing of interfaces upon closure.

Finally, the normal traction is modified as in [55],

$$t_n = e\frac{\sigma_c}{\alpha}\sinh(\frac{\alpha\delta_n}{\delta_c}) \quad \text{if } \delta_n < 0, \tag{25}$$

as a simple method to avoid interface interpenetration. This repulsive traction rapidly increases for $\alpha \approx 100$ and results in a C^1-continuous normal traction response.

3.2 Continuum damage model

The isotropic continuum damage model presented by Simo and Ju [56] is adopted for modeling failure of phases. The damage model is based on the free energy potential

$$\psi\left(\boldsymbol{\epsilon}, \omega\right) = \left(1-\omega\right)\psi_0\left(\boldsymbol{\epsilon}\right), \tag{26}$$

where ψ_0 is the elastic stored energy of the undamaged material, which for the current case of linear isotropic elasticity, is given by

$$\psi_0\left(\boldsymbol{\epsilon}\right) = \frac{1}{2}\boldsymbol{\epsilon} : \boldsymbol{D}_0 : \boldsymbol{\epsilon}, \tag{27}$$

with $\boldsymbol{D}_0$ indicating the linear elasticity tensor. For the isothermal case, this model corresponds to a stress tensor expressed as

$$\boldsymbol{\sigma} = \left(1-\omega\right)\boldsymbol{D}_0 : \boldsymbol{\epsilon}. \tag{28}$$

The Clausius-Duhem inequality for this system is

$$\psi_0 \dot{\omega} \geq 0, \tag{29}$$

which implies that $\dot{\omega} \geq 0$ as ψ_0 is a quadratic function. The onset of damage can be described by the yield surface function

$$g(\psi_0, \omega^t) = G(\psi_0) - \omega^t, \tag{30}$$

where ω^t indicate the damage at time t. A three-parameter Weibull distribution is used for the G function as in [57] and [58]

$$G(\psi_0) = 1 - \exp\left[-\left(\frac{\psi_0 - Y_{in}}{p_1 Y_{in}}\right)^{p_2}\right]. \tag{31}$$

This choice of yield function allows for a wide range of nonlinear responses of materials from ductile to brittle.

The evolution equation for the damage is chosen to be

$$\dot{\omega} = \mu \left\langle g(\psi_0, \omega) \right\rangle, \tag{32}$$

which introduces a viscous dependence on the damage as in [56] to avoid the loss of material ellipticity that may occur in rate-independent evolution models, thereby avoiding mesh bias in the computational solution. μ is a damage consistency parameter, and the $\langle\rangle$ operator denotes Macaulay brackets indicating damage evolution only after the function g becomes positive.

When continuum damage is modeled using the EHM, damage is represented by one internal damage variable in each phase part. The discretization of the damage evolution equation in time gives the residual update equation in part α,

$${}^{n}\omega^{[\alpha]} - \frac{\left({}^{n-1}\omega^{[\alpha]} + \mu \Delta t G(\psi_0(\boldsymbol{\epsilon}))\right)}{1 + \mu \Delta t} = 0, \tag{33}$$

which advances the damage value using a backward Euler integration scheme. ${}^{n-1}\omega^{[\alpha]}$ is the damage in phase part α at at the beginning of the time step and ${}^{n}\omega^{[\alpha]}$ is the updated damage variable. Δt is the time step taken by the incremental nonlinear solver.

4 Model Verification

To verify the formulation presented in Sections 2 and 3, three convergence studies are presented here using a microstructure containing a single spherical inclusion of radius 35 μm inside a cubic PUC with sides of length 100 μm. Damage inside the spherical inclusion, damage

in the surrounding matrix, and debonding of the inclusion/matrix interface are considered separately in this ROM convergence study to assess the impact of the type of damage on the precision and efficiency of the ROM. The damageable domain is partitioned into ROM parts at various levels of refinement and the stress-strain response obtained from the IGFEM-based EHM is compared to the response obtained from a full reference IGFEM simulation for both pure shear and biaxial loading cases. The elastic properties of the spherical inclusion are isotropic in all simulations with parameters $E_i = 12$ GPa and $\nu_i = 0.4$. The matrix is isotropic as well with elastic properties $E_m = 2.4$ GPa and $\nu_m = 0.4$, characteristic of an epoxy matrix. For the reference simulation and the preprocessing of the EHM using IGFEM, the microstructure is meshed using a non-conforming grid of linear tetrehedral elements with a total of 20,480 elements and 6299 nodes, 1386 of which are enrichment nodes.

All simulations presented in this section involve a macroscopic strain loading applied in 50 equally sized load increments. As a reference, the full nonlinear IGFEM solutions are computed using a quasi-Newton-Raphson (qNR) method by default and a full NR step when the qNR fails to converge, which limits the number of costly matrix factorizations. Stiffness matrices are factored with a parallel Cholesky algorithm in the MUMPS package supplied by the PETSc library [59]. ROM solutions are also computed using this methodology, though the resulting dense matrices are solved using the GNU scientific library [60] in serial. Both IGFEM and EHM are implemented in the in-house package Par-IGFEM [61].

The two measures used to evaluate the accuracy and efficiency of the ROM are the relative error and the speedup defined as

$$Error_{L2} = \sqrt{\frac{\int_0^{\epsilon^*} \left(\bar{\sigma}^*_{ROM} - \bar{\sigma}^*_{IGFEM}\right)^2 d\epsilon}{\int_0^{\epsilon^*} \left(\bar{\sigma}^*_{IGFEM}\right)^2 d\epsilon}}, \tag{34a}$$

$$Speedup = \frac{t_{IGFEM}}{t_{ROM}}, \tag{34b}$$

where $*$ indicates the stress or strain component of interest, t_{IGFEM} is the walltime to compute the nonlinear IGFEM response, and t_{ROM} is the walltime to compute the nonlinear evaluation of the ROM response. The preprocessing time for the ROM has not been included here as it can be amortized over many ROM evaluations using different loading cases or nonlinear models with no additional preprocessing required. This preprocessing represents less than 5% of t_{IGFEM} for all examples presented hereafter.

4.1 Damage in inclusion

For the convergence study presented in this section, the nonlinear material response is associated with damage present inside the spherical inclusion. The damage parameters entering

(31) are $Y_{in} = 0.15\,MPa$, $P_1 = 5$, $P_2 = 0.5$, and $\mu = 20\,s^{-1}$.

The 3D PUC is subjected to pure shear and biaxial tension loads: $\bar{\epsilon}_{shear} = \{0, 0, 0, 0, 0, 0.04\}$ and $\bar{\epsilon}_{biaxial} = \{0.04, 0.04, 0, 0, 0, 0\}$. The homogenized response curves for the stress components of interest (σ_{xy} and σ_{xx}, respectively) are presented in Figures 3a and 3b. Both show remarkable agreement with the full IGFEM response with all relative errors falling below 0.5%, even with a single part used. Figure 3c shows the dependence of the L_2 error on the number of parts in the inclusion, as well as the evolution of the speedup. A 600x speedup is achieved for ROM partitionings with 8 parts or fewer. Although this speedup decreases when the number of ROM parts is increased, speedups of over 100x are still obtained with 64 parts, for which the error for shear loading is below 0.08% and the error for biaxial loading is below 0.42%.

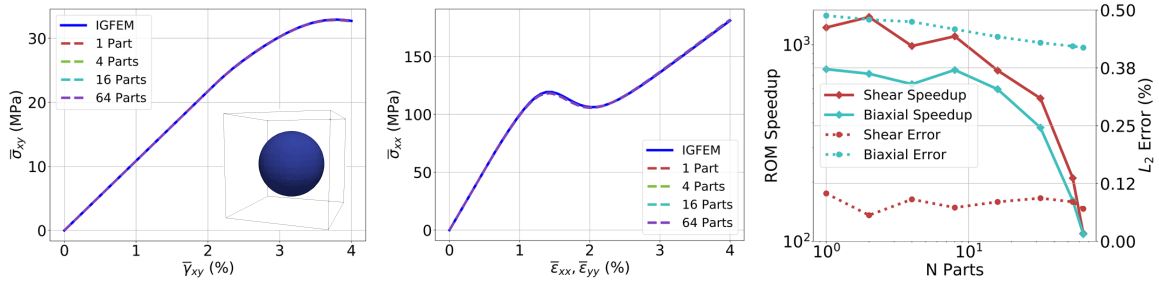

Figure 3: Convergence study of the IGFEM-based EHM for the case of in-inclusion damage. (a) Pure shear response. (b) Biaxial tension response. (c) Speedups and errors for both shear and biaxial ROM loadings.

4.2 Cohesive debonding

In the second convergence study, all phases are assumed to be linearly elastic and the nonlinear response of the particulate composite is associated with the debonding of the inclusion from the surrounding matrix based on the traction-separation model described in Section 3.1. The cohesive model parameters chosen here are $\sigma_c = 100\,MPa$ and $\delta_c = 20\,nm$.

Figure 4a depicts the domain response in pure shear with $\bar{\gamma}_{xy} = 0.08$. The IGFEM shows a sharp drop in the $\bar{\sigma}_{xy}$ response of nearly 15 MPa near $\bar{\gamma}_{xy} = 0.06$. Coarser ROM partitionings do not capture this drop but models with 16 or more interface parts exhibit a stress drop that progressively converges toward the IGFEM response. Figure 4b shows that a similar response is obtained in the biaxial case with $\bar{\epsilon}_{xx} = \bar{\epsilon}_{yy} = 0.02$, where the ROM more accurately captures the ∼40 MPa stress drop in the homogenized response predicted by the full IGFEM solution. The 128-part model captures this behavior well, while coarser partitionings overestimate the strain at which the drop occurs leading to an overshoot of the

peak stress estimate. The evolution of the relative errors and speedups in Figure 4c shows that a larger number of interface parts are required to achieve lower error than in the inclusion damage case described in the previous subsection, likely due to the near-discontinuous nature of the response. It should be noted, however, that the 128-interface-part models still achieve errors of 8% in shear and 5% in biaxial tension with speedups of over 500x.

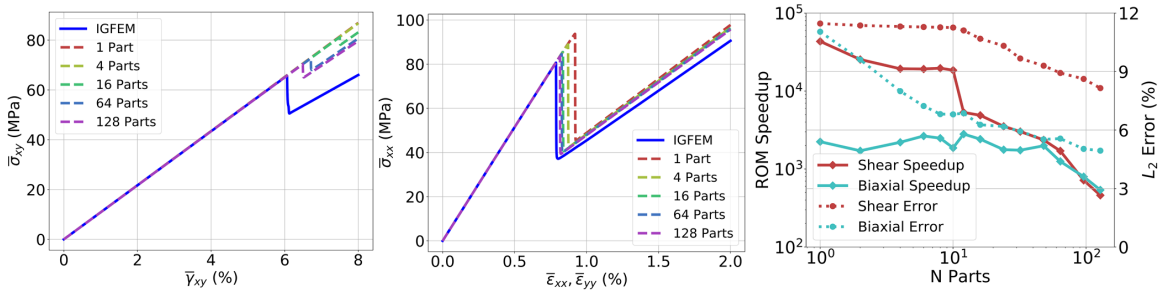

(a) (b) (c)

Figure 4: Convergence study of the IGFEM-based EHM examining cohesive debonding of the particle from the matrix. (a) Pure shear response. (b) Biaxial tension response. (c) Dependence of the speedup and relative error on the number of interface parts.

4.3 Matrix damage

The final nonlinear response investigated here is the case of continuum damage occurring in the matrix with damage parameters $Y_{in} = 0.15$ MPa, $P_1 = 15$, $P_2 = 0.4$, and $\mu = 20\ s^{-1}$. This set of parameters ensures no softening of the macroscopic stress-strain response, thereby maintaining the separation-of-scales assumption that underlies the homogenization formulation (1).

The stress-strain response in pure shear is shown in Figure 5a. The ROM-predicted response is similar to its IGFEM counterpart, both exhibiting a flattening of the homogenized stress-strain curve near $\bar{\gamma}_{xy} = 0.015$ followed by a monotonically increasing response. The convergence toward the IGFEM solution in the shear loading as well as in the biaxial loading response (Figure 5b) is monotonic as exhibited by the error plot in Figure 5c. The high cost of the IGFEM evaluation in this case also leads to very high speedups. At a 3% error level, the shear case achieves a 10,000x speedup while the biaxial model is almost 1000x faster than the full IGFEM. The quick convergence of the ROM solution, along with a relatively flat speedup curve, indicate that modest levels of error can be achieved while obtaining remarkably fast results.

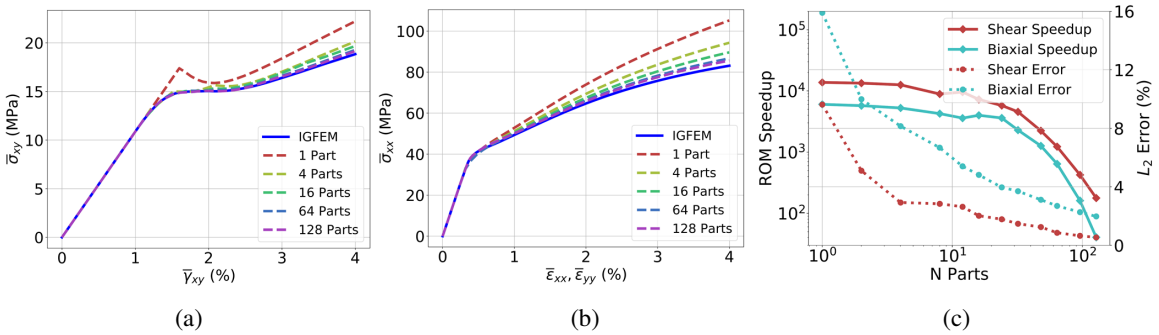

(a) (b) (c)

Figure 5: Convergence study of the IGFEM-based EHM with nonlinear damage in the matrix. (a) Pure shear response. (b) Biaxial tension response. (c) Speedups and errors for both shear and biaxial ROM loadings as a function of number of matrix parts.

5 Application to More Complex Microstructures

5.1 3D particulate composites

The attractiveness of combining IGFEM with the continuum and interface EHM lies in the geometrical flexibility of IGFEM and the computational efficiency of the ROM, which enables the study of PUCs with complex geometries and a wide range of nonlinear damage models. In the example presented hereafter, we compute the homogenized response of ten realizations of a particulate composite PUC composed of ten randomly distributed spherical particles. Each particle has a radius of 3.5 μm and the particle volume fraction for each microstructure is 25.2%. One of these microstructures is presented in Figure 6a, which also illustrates the periodic wrapping of the inclusions. The reference nonlinear IGFEM response of these ten PUCs is simulated as in Section 4 for a macroscopic strain load of $\bar{\epsilon} = \{0.04, -0.01, -0.01, 0, 0, 0\}$ applied in 50 equally sized load steps. These solutions are computed using four processors with an average of 101,392 nonlinear degrees-of-freedom per problem. The preprocessing steps for all ROMs are also conducted using four processors. The elastic properties of all phases are the same as in Section 4.

First, damage in the matrix phase is investigated. Figure 6b shows the matrix damage model selected because it does not exhibit significant softening, thereby maintaining the separation of scales. Several partitionings of the matrix phase were examined in this study. Figure 6c presents the 4-part clustering of the matrix phase, showing that the various parts are allocated to regions with similar values of the strain concentration tensor.

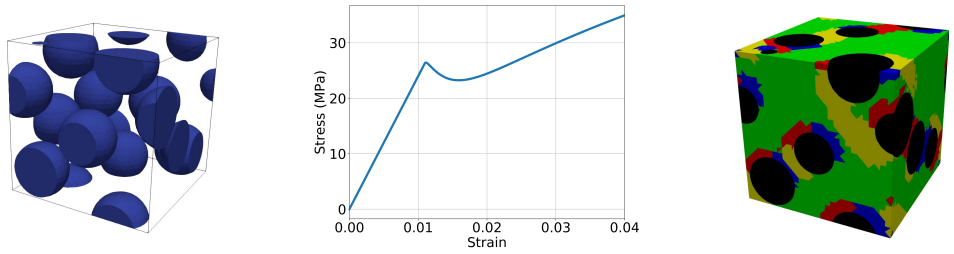

(a) (b) (c)

Figure 6: Setup of ROM of a 10-spherical-particle microstructure with matrix failure. (a) One of 10 microstructures. (b) 1-D damage response of the matrix phase under uniaxial stress loading. (c) 4-part clustering of the matrix phase.

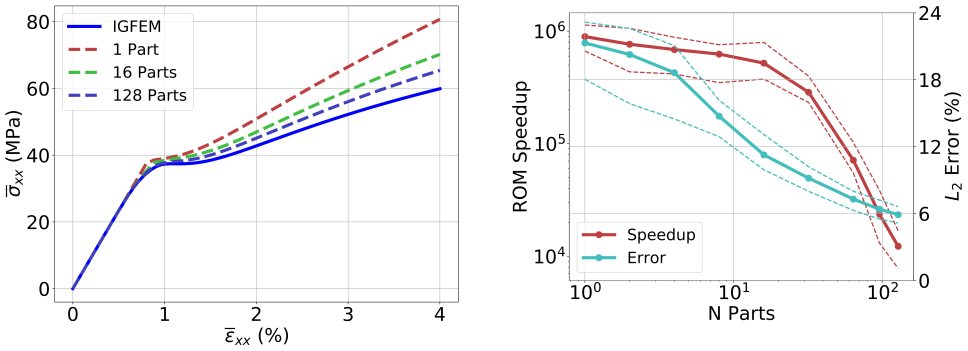

(a) (b)

Figure 7: ROM simulation of the homogenized response of of 10-spherical-particle microstructures in the presence of matrix failure. (a) Macroscopic stress-strain curve for of one of the 10 simulated geometries. (b) Average relative errors and speedups for the 10 geometries with the minimum and maximum values at each level of ROM partitioning denoted by dashed bounds.

Figure 7a shows the IGFEM $\bar{\sigma}_{xx} - \bar{\epsilon}_{xx}$ curves and selected ROM stress responses from one of the ten microstructures. All ROM responses exhibit trends similar to the reference direct IGFEM solution, with the ROM solutions progressively approaching the IGFEM curve as the number of parts used in the matrix phase increases. Figure 7b shows the dependence of the relative error and ROM speedup values on the number of parts. The minimum and maximum errors and speedups for each ROM are shown with dashed curves. Speedups in excess of 300,000x are possible with errors <18% or ∼10,000x with 6% error. These very large speedups are primarily due to the larger size of the finite element problems compared to the verification problems presented in Section 4. As shown in Figure 8, the ϵ_{xx} fields obtained from the direct IGFEM simulation and from the 128-part ROM are visually similar with the same patterns of strain concentrations. Note, however, that while the IGFEM contour plot is readily available from the IGFEM simulation, the full ROM perturbation displacement field

must be obtained from a post-processed linear combination of the influence functions with the $\mu^{[\alpha]}$ and $\delta^{[\xi]}$ coefficients.

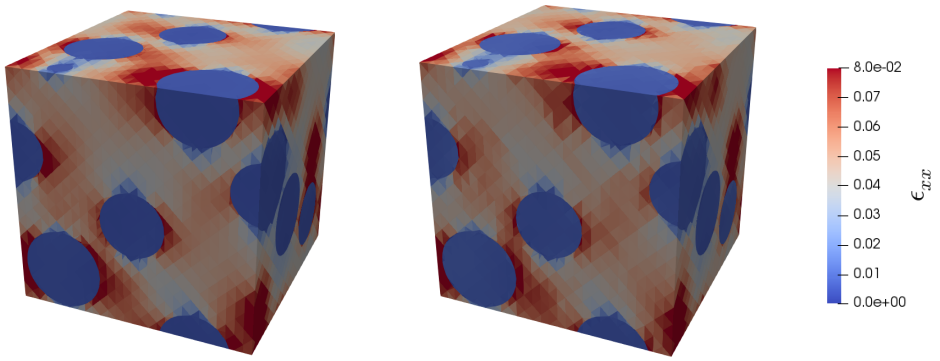

Figure 8: Comparison between the strain fields obtained with the full IGFEM simulation (left) and the ROM solution with 128 parts in the matrix phase (right).

Damage inside of the inclusions is investigated next, with the 1-D nonlinear response of the inclusion damage model exhibiting the semi-brittle behavior shown in Figure 9a. Figure 9b depicts the partitioning of the inclusions into four ROM parts. There does not appear to be a discernible pattern in the partitioning but all four regions seem to be approximately evenly distributed.

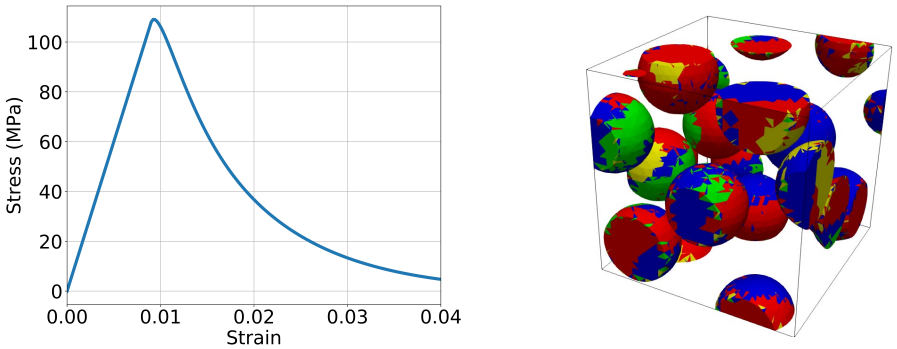

(a) (b)

Figure 9: Setup of ROM of 10-spherical particle microstructures with inclusion phase failure. (a) Uniaxial stress-strain response of the inclusion material, showing a semi-brittle response. (b) Coloring of the parts when the inclusion phase is split into 4 parts.

The stress response in Figure 10a shows remarkable agreement between the ROM approximation and the reference IGFEM simulation, which is consistent with the results summarized in Section 4.1. The damage response of the inclusions results in a drop in the macroscopic stress of nearly 30 MPa starting near $\bar{\epsilon}_{xx} = 2.25\%$ followed by a stress recovery from $\bar{\epsilon}_{xx} = 3.5\%$. The dependence of the average relative error on the number of parts used

inside the inclusions is shown in Figure 10b with the minimum and maximum limits shown as dashed bounds. Relative errors below 2% are achieved with speedups of over 10,000x in the worst case observed.

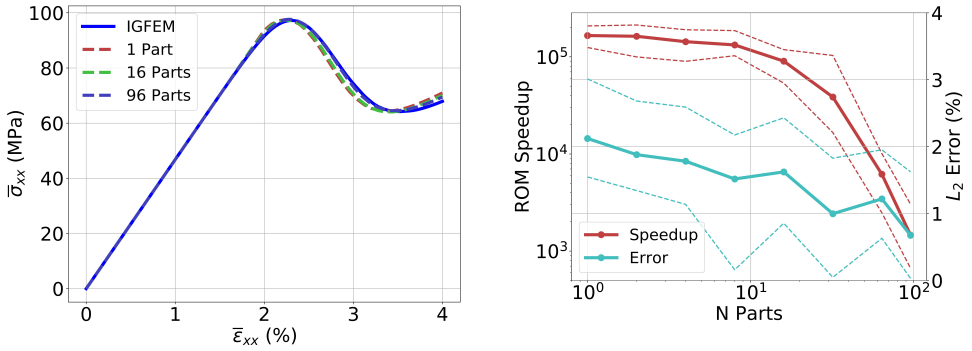

(a) (b)

Figure 10: ROM simulation of 10-spherical particle microstructures with inclusion phase failure. (a) Stress-strain results of one of the ten geometries tested. (b) Dependence of the relative errors and speedups on the number of ROM parts used. Dashed lines denote minimum and maximum observed.

The final failure case examined for the 10-spherical-particle PUC involves the cohesive debonding of the inclusions. The Ortiz-Pandolfi CZM described in Section 3.1 is used with parameters $\sigma_c = 25\ MPa$ and $\delta_c = 25\ nm$ and only one geometry is studied. Figure 11a shows the distribution of 16 interface parts across all ten particle surfaces. Similarly oriented regions of different particles are assigned to the same interface ROM part, indicating that most inclusion interfaces are behaving similarly in the initial elastic response.

Figure 11b shows the macroscopic stress-strain response of the reference IGFEM simulation and select partitionings of the ROM. ROMs with few parts vastly overpredict the stress after the initial failure near $\bar{\epsilon}_{xx} = 0.015$ compared to the full IGFEM, but addition of more parts to the ROM decreases this overestimation. The use of 512 parts leads to a relative error of ~20% as seen in Figure 11c. This slow convergence may be because cohesive failure is often highly localized and restricting interface regions across multiple inclusions to behave similarly via the partitioning limits the ability for this localization to occur. The similarity of interface regions' initial elastic response may not necessarily be a good indicator of the debonding behavior later in the simulation. The simple geometry in Section 4.2 did not suffer from this as it only contained one particle. However, moderate levels of error in this more complex PUC can still be achieved at a faster speed than the full IGFEM as the 512-part model obtains a speedup of 87x.

The possibility that the sliver elements mentioned in Section 2.2 caused the relatively

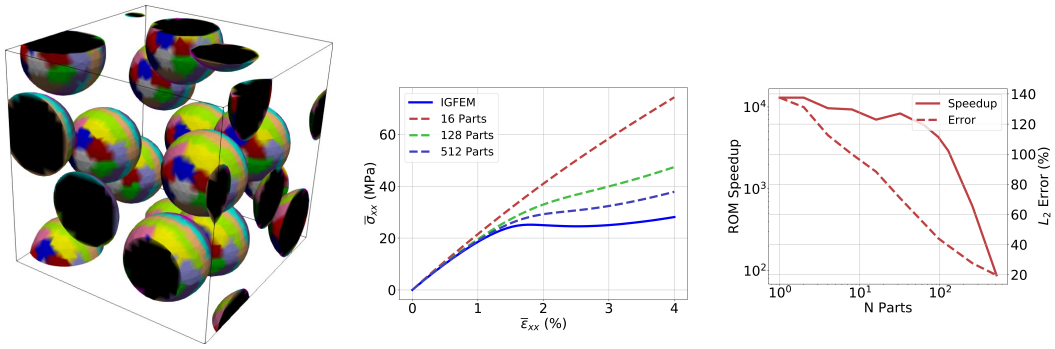

(a) (b) (c)

Figure 11: Setup of ROM of a 10-spherical particle microstructure with cohesive debonding. (a) The 10-sphere geometry with the surface of each particle colored by the interface part numbers. (b) Homogenized stress-strain response of select ROM solutions compared to the IGFEM reference solution. (c) Dependence of the ROM error and speedup on the number of interface parts.

large error for the case of cohesive debonding is investigated by examining the local stress states. The von Mises stress fields obtained from the full IGFEM solution (Fig. 12 (a)) and the 512-part cohesive ROM (Fig. 12 (b)) along the plane (z=0.00525mm) intersecting multiple inclusions show very similar stress patterns, especially in the matrix region. The presence of sliver elements adjacent to the material interfaces do not appear to affect the stress solution associated with the IGFEM. The stress irregularities present along the material interfaces in the ROM appear therefore to be caused by interface part boundaries rather than poorly conditioned elements. These irregular stress peaks may be alleviated using recovery or averaging methods [62, 63]. The spatial variation of the IGFEM and ROM solutions for the von Mises stress along two straight paths (denoted by the black horizontal lines in Fig. 12 (a) and (b)) is presented in Fig. 12 (c). A comparison between the IGFEM (solid curves) and ROM (dashed curves) solutions shows a good overall agreement especially along the path limited to the matrix (blue curves). The difference between IGFEM and ROM solutions are more noticeable for the (lower) path crossing two inclusions, whose location is denoted by the shaded regions in Fig. 12 (c). More than the presence of stress peaks in the ROM solution immediately adjacent to the material interfaces due to the interface part boundaries, the overall gap between the solid and dashed curves in the PUC is the primary cause of the error in the homogenized stress-strain solution.

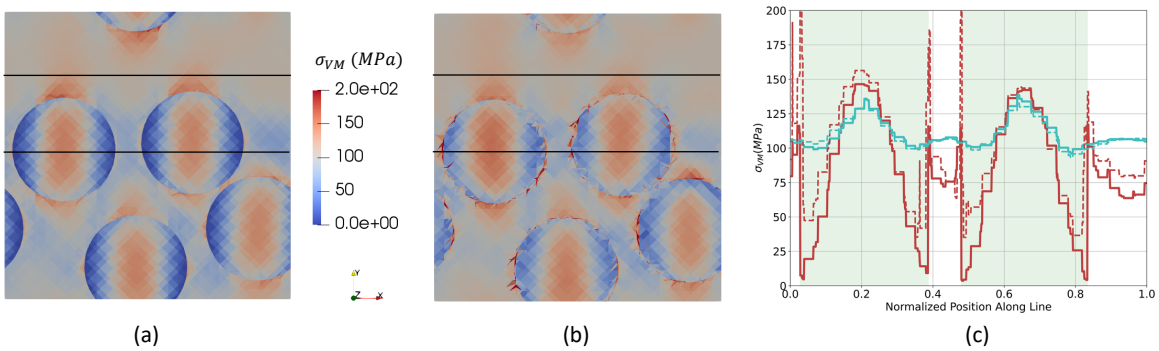

Figure 12: Von Mises stress field in (a) the full IGFEM solution and (b) the 512-interface part ROM. (c) Spatial variation of the Von Mises stress solution obtained along the horizontal lines shown in (a) and (b) by the IGFEM (solid curves) and ROM (dashed curves) solvers. The red and blue curves respectively correspond to the lower and upper paths. The shaded regions denote the location of the inclusions traversed by the lower line, where the von Mises stress solution (red curves) experiences jumps.

5.2 Transverse failure of a composite ply

IGFEM's ability to capture complex geometries is demonstrated here by modeling the 2D domain shown in Figure 13a which represents the cross-section of a unidirectional ply of a composite laminate containing 575 circular fibers at $\sim 60\%$ fiber volume fraction. The continuum damage model depicted in Figure 6b is applied to the matrix phase and the domain is subjected to a pure shear loading with $\bar{\gamma}_{xy} = 0.03$. The entire domain contains 236,412 triangular elements and 331,134 degrees-of-freedom, with both the IGFEM solution and the ROM preprocessing computed on 4 processors.

Figure 13b shows the macroscopic $\bar{\sigma}_{xy} - \bar{\gamma}_{xy}$ response. As alluded to in in Section 4.3, diffuse matrix failure is captured very well with only a few ROM parts, as illustrated by the result obtained with the 16-part model which achieves an 8% relative error with a 90,000x speedup. The local shear stress distributions in the reference IGFEM and the 256-ROM are compared in Figure 14, with both showing similar shear stress patterns.

5.3 Woven composite PUC

The final microstructure studied in this work is a woven composite PUC consisting of four woven, sinusoidally varying fiber tows with elliptical cross sections. The geometry of the domain is shown in Figure 15a with the primary axis of two tows oriented in the x-direction and the remaining two tows in the perpendicular direction. The tows are assumed to be linear

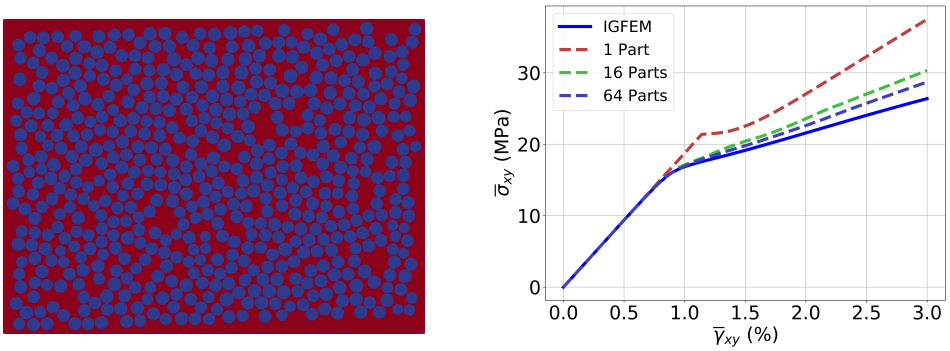

(a) (b)

Figure 13: Shear loading of a transverse composite layer with matrix damage. (a) 575-fiber composite ply geometry. (b) IGFEM and ROM predictions of the homogenized shear response.

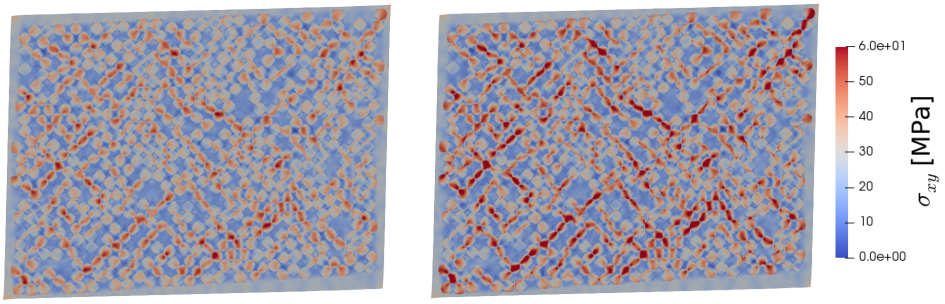

Figure 14: Comparison of the shear stress fields in the full IGFEM simulation (left) and the 256-part ROM simulation (right).

elastic and transversely isotopic with the principal axis parallel to the tow centerline. Their properties are $E_1 = 49.2$ GPa, $E_2 = 7.2$ GPa, $G_{12} = 4$ GPa, $G_{23} = 2$ GPa, and $\nu_{12} = 0.3$, which are equivalent to the properties of a glass fiber-epoxy composite with a fiber volume fraction of 60%. The elastic properties of the matrix material are the same as in Section 4. The computational domain contains 232,320 linear tetrahedral elements and 315,357 degrees-of-freedom with all IGFEM preprocessing and reference IGFEM computations completed on 8 processors. Damage in the matrix region combined with cohesive debonding of the tows from the surrounding matrix is considered in this section. The matrix damage model utilizes the parameters $Y_{in} = 0.15$ MPa, $p_1 = 20$, and $p_2 = 0.8$ while the tow/matrix interface CZM parameters are $\sigma_c = 50$ MPa and $\delta_c = 5\,\mu m$.

Figure 15a shows the interface part distribution for the 16-interface-part case. It again clearly shows the assignment of similar regions of the microstructure to the same interface part, while allowing for clustering of parts in regions of high curvature or high strain-concentration. Figure 15b shows the distribution of 16 parts in the matrix phase region with similar regions again being grouped together.

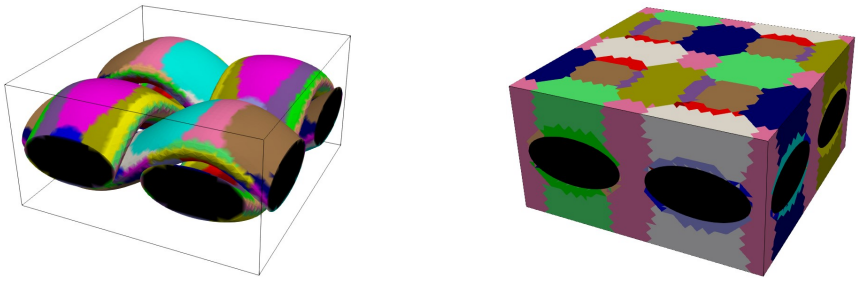

(a) (b)

Figure 15: (a) 16 interface parts on woven composite geometry. (b) 16 phase parts in the matrix of the woven PUC.

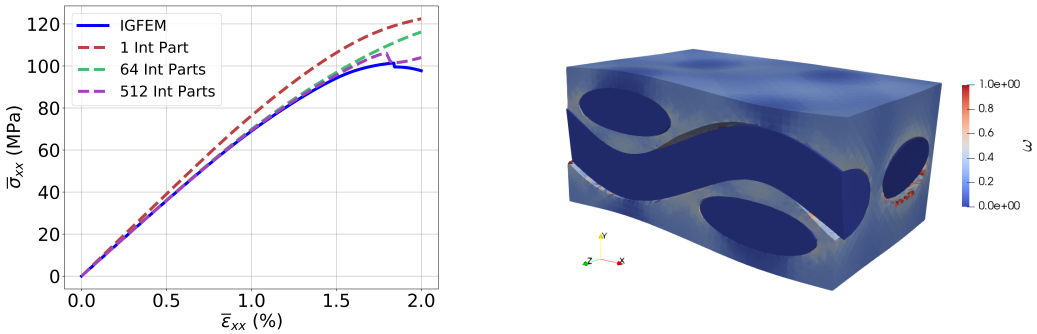

(a) (b)

Figure 16: Woven composite with matrix damage and interface failure. All ROMs use 64 matrix parts. (a) Macroscopic stress-strain response. (b) Distribution of the damage parameter ω in a deformed section of the 64-matrix/512-interface-part ROM PUC also showing debonding along the fiber-tow/matrix interface. Deformations have been emphasized by 5x.

The results of loading this PUC of the woven composite to $\bar{\epsilon} = \{[0.02, -0.005, -0.005, 0, 0, 0]\}$ are presented in Figure 16. Figure 16a shows the homogenized stress response of the ROM with 64 matrix parts and varying numbers of interface ROM parts compared to the IGFEM reference simulation. Again, relatively large numbers of interface parts are necessary to capture the full nonlinear behavior but substantial computational savings are still achieved with the 64-matrix/512-interface part model running at a 843x speedup. The gradual reduction in stiffness of the composite is captured as well as the drop in stress that occurs at the peak of the homogenized stress-strain curve. Figure 16b shows a slice through the final deformed configuration of the PUC with a diffuse damage field in the matrix region and substantial interfacial debonding of the tows from the matrix.

6 Summary

This work has developed a reduced-order model based on combining the eigendeformation-based reduced-order homogenization model (EHM) and the Interface-enriched Generalized Finite Element Method (IGFEM), which efficiently provides an approximation of the multiscale nonlinear constitutive response of PUCs with complex geometries. The use of continuum damage models and cohesive interfaces separately and simultaneously allows for a diverse set of nonlinear behaviors to be analyzed. The ability to use the same preprocessing phase of the EHM for varying nonlinear model parameters makes it an efficient tool for analyzing multiple macroscopic loadings of a domain or investigating the statistical variation of the model response with respect to the material parameters. The IGFEM introduces flexibility with respect to the geometrical parameters as well since the mesh is independent of the material interface geometry, readily allowing for analyses of many periodic unit cells (PUCs) with variation of the geometry as well.

A method of interface constraints for the efficient elastic preprocessing of the ROM was developed using Lagrange multipliers, which allowed for the reuse of the stiffness matrix factorization in the Elastic, Phase, and Interface Influence Function problems. A modified traction integration scheme was also presented to address the numerical instability associated with the IGFEM evaluation of the interface tractions. Finally, a deformation-based k-means clustering approach was developed to optimally partition the domain into phase and interface parts using the strain concentration tensor and the displacement jump concentration matrix.

Speedups of several orders of magnitude were achieved at moderate levels of error compared to a reference IGFEM solution for most nonlinear model cases. However, assumptions made in the partitioning approach limit the accuracy in highly localized failure processes. Additionally, the number of parts required to capture interfacial failure accurately for larger microstructures appears to be significantly higher than that needed to capture damage in the matrix or reinforcement phases, increasing the computational cost of simulations involving debonding processes.

The IGFEM-based EHM can be further improved by adopting partitioning schemes that allow for more complex failure paths or are geometry- or loading-specific. The ROM approach described in this manuscript provides a powerful tool to simulate PUCs in coupled multiscale FE^2 simulations or in the calibration of nonlinear model parameters. The independence of the preprocessing stage from the nonlinear model parameters also makes this tool useful for the multiscale design of material microstructures to achieve specified nonlinear homogenized constitutive responses. While the computational gains might be lessened by including geometrical parameters in the nonlinear design process due to the need to recalculate the coefficient tensors, savings might still be achieved over full nonlinear IGFEM analyses.

Acknowledgements

Support from the National Science Foundation Graduate Research Fellowship Program under Grant No. DGE - 1144245 is gratefully acknowledged. Additional support was provided to DB by an Illinois Distinguished Fellowship from the Graduate College at the University of Illinois at Urbana-Champaign, and the start-up funding to XZ provided by the University of Wyoming

References

[1] J. A. Nairn, Matrix Microcracking in Composites, in: A. Kelly, C. Zweben (Eds.), Comprehensive Composite Materials Volume 2: Polymer Matrix Composites, Elsevier Ltd, 2000, Ch. 12, pp. 403–432.

[2] I. Babuška, Homogenization and its application. Mathematical and computational problems, in: Numerical Solution of Partial Differential Equations–III, Academic Press, 1975, pp. 89–116. doi:10.1016/B978-0-12-358503-5.50009-9.

[3] A. Bensoussan, J.-L. Lions, G. Papanicolaou, Asymptotic Analysis for Periodic Structures, Vol. 5, American Mathematical Society, 1978. doi:10.1016/S0168-2024(08)70198-X.

[4] E. Sanchez-Palencia, Homogenization method for the study of composite media, in: Asymptotic Analysis II, Lecture Notes in Mathematics, Springer, 1983, pp. 192–214. doi:10.1007/BFb0062368.

[5] J. M. Guedes, N. Kikuchi, Preprocessing and postprocessing for materials based on the homogenization method with adaptive finite element methods, Computer Methods in Applied Mechanics and Engineering 83 (1990) 143–198. doi:10.1016/0045-7825(90)90148-F.

[6] G. J. Dvorak, Transformation field analysis of inelastic composite materials, Proceedings of the Royal Society A: Mathematical, Physical and Engineering Sciences 437 (1992) 311–327. doi:10.1098/rspa.1992.0063.

[7] S. Ghosh, K. Lee, S. Moorthy, Two scale analysis of heterogeneous elastic-plastic materials with asymptotic homogenization and Voronoi cell finite element model, Computer Methods in Applied Mechanics and Engineering 132 (1) (1996) 63–116. doi:10.1016/0045-7825(95)00974-4.

[8] C. Miehe, J. Schröder, J. Schotte, Computational homogenization analysis in finite plasticity simulation of texture development in polycrystalline materials, Computer Methods in Applied Mechanics and Engineering 171 (1999) 387–418. doi:10.1016/S0045-7825(98)00218-7.

[9] F. Feyel, J.-L. Chaboche, FE2 multiscale approach for modelling the elastoviscoplastic behaviour of long fibre SiC/Ti composite materials, Computer Methods in Applied Mechanics and Engineering 183 (2000) 309–330. doi:10.1016/S0045-7825(99)00224-8.

[10] K. Matouš, M. G. Geers, V. G. Kouznetsova, A. Gillman, A review of predictive nonlinear theories for multiscale modeling of heterogeneous materials, Journal of Computational Physics 330 (2017) 192–220. doi:10.1016/j.jcp.2016.10.070.

[11] M. Mosby, K. Matouš, Computational homogenization at extreme scales, Extreme Mechanics Letters 6 (2016) 68–74. doi:10.1016/j.eml.2015.12.009.

[12] Rahul, S. De, Analysis of the Jacobian-free multiscale method (JFMM), Computational Mechanics 56 (5) (2015) 769–783. doi:10.1007/s00466-015-1200-z.

[13] J. Yvonnet, Q. He, The reduced model multiscale method (r3m) for the non-linear homogenization of hyperelastic media at finite strains, Journal of Computational Physics 223 (1) (2007) 341–368. doi:10.1016/j.jcp.2006.09.019.

[14] J. A. Hernández, J. Oliver, A. E. Huespe, M. A. Caicedo, J. C. Cante, High-performance model reduction techniques in computational multiscale homogenization, Computer Methods in Applied Mechanics and Engineering 276 (2014) 149–189. doi:10.1016/j.cma.2014.03.011.

[15] H. Moulinec, P. Suquet, A numerical method for computing the overall response of nonlinear composites with complex microstructure, Computer Methods in Applied Mechanics and Engineering 157 (1998) 69–94. doi:10.1016/S0045-7825(97)00218-1.

[16] L. Sharma, R. H. Peerlings, P. Shanthraj, F. Roters, M. G. Geers, An FFT-based spectral solver for interface decohesion modelling using a gradient damage approach, Computational Mechanics (2019) 1–15doi:10.1007/s00466-019-01801-4.

[17] Z. Liu, M. A. Bessa, W. K. Liu, Self-consistent clustering analysis: An efficient multi-scale scheme for inelastic heterogeneous materials, Computer Methods in Applied Mechanics and Engineering 306 (2016) 319–341. doi:10.1016/j.cma.2016.04.004.

[18] C. Yu, O. L. Kafka, W. K. Liu, Self-consistent clustering analysis for multiscale modeling at finite strains, Computer Methods in Applied Mechanics and Engineering 349 (2019) 339–359. doi:10.1016/j.cma.2019.02.027.

[19] Z. Liu, C. T. Wu, M. Koishi, A deep material network for multiscale topology learning and accelerated nonlinear modeling of heterogeneous materials, Computer Methods in Applied Mechanics and Engineering 345 (2019) 1138–1168. doi:10.1016/j.cma.2018.09.020.

[20] Z. Liu, Deep material network with cohesive layers: Multi-stage training and interfacial failure analysis, Computer Methods in Applied Mechanics and Engineering 363 (2020) 112913. doi:10.1016/j.cma.2020.112913.

[21] J.-C. Michel, P. Suquet, Computational analysis of nonlinear composite structures using the nonuniform transformation field analysis, Computer Methods in Applied Mechanics and Engineering 193 (48-51) (2004) 5477–5502. doi:10.1016/j.cma.2003.12.071.

[22] C. Oskay, J. Fish, Eigendeformation-based reduced order homogenization for failure analysis of heterogeneous materials, Computer Methods in Applied Mechanics and Engineering 196 (7) (2007) 1216–1243. doi:10.1016/j.cma.2006.08.015.

[23] Z. Yuan, J. Fish, Multiple scale eigendeformation-based reduced order homogenization, Computer Methods in Applied Mechanics and Engineering 198 (2009) 2016–2038. doi:10.1016/J.CMA.2008.12.038.

[24] X. Zhang, C. Oskay, Eigenstrain based reduced order homogenization for polycrystalline materials, Computer Methods in Applied Mechanics and Engineering 297 (2015) 408–436. doi:10.1016/j.cma.2015.09.006.

[25] X. Zhang, C. Oskay, Sparse and scalable eigenstrain-based reduced order homogenization models for polycrystal plasticity, Computer Methods in Applied Mechanics and Engineering 326 (2017) 241–269. doi:10.1016/j.cma.2017.07.027.

[26] X. Zhang, Y. Liu, C. Oskay, Coupling crystal plasticity with structural mechanics for prediction of thermo-mechanical response in large scale structures, in: 6th European Conference on Computational Mechanics, Glasgow, UK, 2018.

[27] Y. Liu, X. Zhang, Y. Zhu, P. Hu, C. Oskay, Dislocation density informed eigenstrain based reduced order homogenization modeling: verification and application on a titanium alloy structure subjected to cyclic loading, Modelling and Simulation in Materials Science and Engineering 28 (2) (2020) 025004. doi:10.1088/1361-651X/ab602es.

[28] X. Zhang, Y. Liu, C. Oskay, Multiscale Reduced-Order Modeling of a Titanium Skin Panel Subjected to Thermo-Mechanical Loading, arXiv.arXiv:2011.03907.

[29] Z. Yuan, J. Fish, Are the cohesive zone models necessary for delamination analysis?, Computer Methods in Applied Mechanics and Engineering 310 (2016) 567–604. doi:10.1016/j.cma.2016.06.023.

[30] C. Oskay, Z. Su, B. Kapusuzoglu, Discrete eigenseparation-based reduced order homogenization method for failure modeling of composite materials, Computer Methods in Applied Mechanics and Engineering 359 (2020) 112656. doi:10.1016/j.cma.2019.112656.

[31] S. Soghrati, P. H. Geubelle, A 3D interface-enriched generalized finite element method for weakly discontinuous problems with complex internal geometries, Computer Methods

in Applied Mechanics and Engineering 217 (2012) 46–57. doi:10.1016/j.cma.2011.12.010.

[32] M. Ortiz, A. Pandolfi, Finite-deformation irreversible cohesive elements for three-dimensional crack-propagation analysis, International Journal for Numerical Methods in Engineering 44 (9) (1999) 1267–1282. doi:10.1002/(SICI)1097-0207(19990330)44:9<1267::AID-NME486>3.0.CO;2-7.

[33] V.-T. Phan, X. Zhang, Y. Li, C. Oskay, Microscale modeling of creep deformation and rupture in Nickel-based superalloy IN 617 at high temperature, Mechanics of Materials 114 (2017) 215–227. doi:10.1016/J.MECHMAT.2017.08.008.

[34] O. Giraldo-Londoño, D. W. Spring, G. H. Paulino, W. G. Buttlar, An efficient mixed-mode rate-dependent cohesive fracture model using sigmoidal functions, Engineering Fracture Mechanics 192 (2018) 307–327. doi:10.1016/j.engfracmech.2017.12.016.

[35] G. J. Dvorak, Y. Benveniste, On transformation strains and uniform fields in multi-phase elastic media, Proceedings of the Royal Society A: Mathematical, Physical and Engineering Sciences 437 (1900) (1992) 291–310. doi:10.1098/rspa.1992.0062.

[36] S. Soghrati, A. M. Aragón, C. Armando Duarte, P. H. Geubelle, An interface-enriched generalized FEM for problems with discontinuous gradient fields, International Journal for Numerical Methods in Engineering 89 (8) (2012) 991–1008. doi:10.1002/nme.3273.

[37] S. Soghrati, P. H. Geubelle, A 3D interface-enriched generalized finite element method for weakly discontinuous problems with complex internal geometries, Computer Methods in Applied Mechanics and Engineering 217-220 (2012) 46–57. doi:10.1016/j.cma.2011.12.010.

[38] A. M. Aragon, A. Simone, The discontinuity-enriched finite element method, International Journal for Numerical Methods in Engineering 112 (2017) 1589–1613. doi:10.1002/nme.5570.

[39] X. Zhang, D. R. Brandyberry, P. H. Geubelle, IGFEM-based shape sensitivity analysis of the transverse failure of a composite laminate, Computational Mechanics 64 (5) (2019) 1455–1472. doi:10.1007/s00466-019-01726-y.

[40] M. Shakiba, D. R. Brandyberry, S. Zacek, P. H. Geubelle, Transverse failure of carbon fiber composites: Analytical sensitivity to the distribution of fiber/matrix interface properties, International Journal for Numerical Methods in Engineering 120 (5) (2019) 650–665. doi:10.1002/nme.6151.

[41] S. Zacek, D. Brandyberry, A. Klepacki, C. Montgomery, M. Shakiba, M. Rossol, A. Najafi, X. Zhang, N. Sottos, P. Geubelle, C. Przybyla, G. Jefferson, Transverse Failure of Unidirectional Composites: Sensitivity to Interfacial Properties, Springer International Publishing, Cham, 2020, p. 329–347. doi:10.1007/978-3-030-40562-5_12.

[42] A. M. Aragón, B. Liang, H. Ahmadian, S. Soghrati, On the stability and interpolating properties of the hierarchical interface-enriched finite element method, Computer Methods in Applied Mechanics and Engineering 362 (2020) 112–671. doi:10.1016/j.cma.2019.112671.

[43] D. R. Brandyberry, A. R. Najafi, P. H. Geubelle, Multiscale design of three-dimensional nonlinear composites using an interface-enriched generalized finite element method, International Journal for Numerical Methods in Engineering 121 (12) (2020) 2806–2825. doi:10.1002/nme.6333.

[44] J. Fish, Practical Multiscaling, John Wiley & Sons, Ltd, 2014. doi:10.1007/978-94-009-3489-4.

[45] S. Zhang, C. Oskay, Reduced order variational multiscale enrichment method for elasto-viscoplastic problems, Computer Methods in Applied Mechanics and Engineering 300 (2016) 199–224. doi:10.1016/j.cma.2015.11.020.

[46] S. Marfia, E. Sacco, Computational homogenization of composites experiencing plasticity, cracking and debonding phenomena, Computer Methods in Applied Mechanics and Engineering 304 (2016) 319–341. doi:10.1016/j.cma.2016.02.007.

[47] R. Hu, C. Oskay, Nonlocal homogenization model for wave dispersion and attenuation in elastic and viscoelastic periodic layered media, Journal of Applied Mechanics 84 (3) (2017) 031003. doi:10.1115/1.4035364.

[48] M. J. Bogdanor, C. Oskay, Prediction of progressive fatigue damage and failure behavior of im7/977-3 composites using the reduced-order multiple space-time homogenization approach, Journal of Composite Materials 51 (15) (2017) 2101–2117. doi:10.1177/0021998316665683.

[49] F. Covezzi, S. de Miranda, S. Marfia, E. Sacco, Multiscale analysis of nonlinear composites via a mixed reduced order formulation, Compos. Struct. 203 (2018) 810–825. doi:10.1016/j.compstruct.2018.05.073.

[50] A. Moyeda, J. Fish, Multiscale analysis of solid, waffle, ribbed and hollowcore reinforced concrete slabs, Computer Methods in Applied Mechanics and Engineering 348 (2019) 139–156. doi:10.1016/j.cma.2019.01.022.

[51] P. Sparks, C. Oskay, Identification of optimal reduced order homogenization models for failure of heterogeneous materials, Journal for Multiscale Computational Engineering 11 (2013) 185–200. doi:10.1615/IntJMultCompEng.2013005373.

[52] G. Alaimo, F. Auricchio, S. Marfia, E. Sacco, Optimization clustering technique for PieceWise Uniform Transformation Field Analysis homogenization of viscoplastic composites, Computational Mechanics 64 (6) (2019) 1495–1516. doi:10.1007/s00466-019-01730-2.

[53] S. P. Lloyd, Least squares quantization in PCM, IEEE Transactions on Information Theory 28 (2) (1982) 129–137. doi:10.1109/TIT.1982.1056489.

[54] D. Arthur, S. Vassilvitskii, K-means++: The advantages of careful seeding, Tech. rep., Stanford (2006).

[55] M. G. Kulkarni, P. H. Geubelle, K. Matouš, Multi-scale modeling of heterogeneous adhesives: Effect of particle decohesion, Mechanics of Materials 41 (5) (2009) 573–583. doi:10.1016/j.mechmat.2008.10.012.

[56] J. C. Simo, J. W. Ju, Strain- and stress-based continuum damage models-I. Formulation, International Journal of Solids and Structures 23 (7) (1987) 821–840. doi:10.1016/0020-7683(87)90083-7.

[57] K. Matouš, M. G. Kulkarni, P. H. Geubelle, Multiscale cohesive failure modeling of heterogeneous adhesives, International Journal for Numerical Methods in Engineering 56 (4) (2008) 1511–1533. doi:10.1016/j.jmps.2007.08.005.

[58] A. R. Najafi, M. Safdari, D. A. Tortorelli, P. H. Geubelle, Multiscale design of nonlinear materials using an Eulerian shape optimization scheme, Submitted.

[59] S. Balay, S. Abhyankar, M. F. Adams, J. Brown, P. Brune, K. Buschelman, L. Dalcin, A. Dener, V. Eijkhout, W. D. Gropp, D. Karpeyev, D. Kaushik, M. G. Knepley, D. A. May, L. C. McInnes, R. T. Mills, T. Munson, K. Rupp, P. Sanan, B. F. Smith, S. Zampini, H. Zhang, H. Zhang, PETSc Web page, https://www.mcs.anl.gov/petsc (2019).

[60] M. Galassi, E. Al., GNU Scientific Library Reference Manual, Tech. rep., GNU (2019).

[61] P. Geubelle, D. Brandyberry, M. Safdari, Par-IGFEM user's manual.

[62] C. Daux, N. Moës, J. Dolbow, N. Sukumar, T. Belytschko, Arbitrary branched and intersecting cracks with the extended finite element method, International Journal for Numerical Methods in Engineering (12) 1741–1760. doi:10.1002/1097-0207(20000830)48:12<1741::AID-NME956>3.0.CO;2-L.

[63] N. Moës, T. Belytschko, Extended finite element method for cohesive crack growth, Engineering Fracture Mechanics 69 (7) (2002) 813–833. doi:10.1016/S0013-7944(01)00128-X.